










# Analog Front-End: Circuit of Pulsar-Based Timing Synchronization for the WAMS

Wei Qiu , Member, IEEE, He Yin , Member, IEEE, Liang Zhang , Xiqian Luo , Yuru Wu , Graduate Student Member, IEEE, Kaiqi Sun , Member, IEEE, Wenxuan Yao , Senior Member, IEEE, Shutang You , Member, IEEE, and Yilu Liu , Fellow, IEEE

**Abstract**—The front-end circuit used in the pulsar acquisition of the radio telescope determines the availability of the entire pulsar-based timing framework. However, it would be expensive and resource consuming to use a real radio telescope in the circuit design process. To address this issue, in this article, the hardware-in-the-loop simulation solution is proposed to generate, sample, and extract pulse signals in real time. The artificial pulse generation method is first proposed to generate the pulses that are close to real pulsar signals. Then, three analog front-end circuit architectures (AFCAs) are proposed to generate the analog pulses, including the superposition, attenuator, and attenuator-based superposition structures. The generated pulses are close to the real pulsar signal in shape, amplitude, and noise level. Next, a pulsar-based timing synchronization framework that can be used to improve the timing accuracy of the wide-area monitoring systems is developed to process the sampled data. Multiple experiments are conducted to verify the effectiveness of the analog front-end and the pulsar-based timing synchronization framework using the simulated pulse and real pulsar signals. The results demonstrated that the designed AFCAs can generate effective analog pulses, and is convenient and flexible.

**Index Terms**—Analog front-end circuit architectures (AFCAs), hardware-in-the-loop, pulsar-based timing synchronization, timing accuracy.

Manuscript received July 29, 2021; revised November 14, 2021; accepted November 16, 2021. Date of publication January 25, 2022; date of current version March 20, 2022. Paper 2021-PSEC-0960.R1, presented at the 2021 IEEE Industry Applications Society Annual Meeting (IAS), Vancouver, BC Canada, Oct. 10–14, and approved for publication in the IEEE TRANSACTIONS ON INDUSTRY APPLICATIONS by the Power Systems Engineering Committee of the IEEE Industry Applications Society. This work was supported in part by the Major Research Instrumentation Program of the National Science Foundation under the Award 1920025, in part by the Engineering Research Center Program of the National Science Foundation under NSF Award EEC-1920025, and in part by the Department of Energy and the CURENT Industry Partnership Program, and in part by the National Natural Science Foundation of China under the Award 52177078. (Corresponding author: He Yin.)

Wei Qiu, He Yin, Liang Zhang, Xiqian Luo, Yuru Wu, and Shutang You are with the Department of Electrical Engineering and Computer Science, The University of Tennessee, Knoxville, TN 37996 USA (e-mail: qiuwei@hnu.edu.cn; hyin8@utk.edu; lzhan104@utk.edu; xlou18@utk.edu; ywu70@vols.utk.edu; syou3@utk.edu).

Kaiqi Sun is with the School of Electrical Engineering, Shandong University, Jinan 250100, China (e-mail: ksun8@utk.edu).

Wenxuan Yao is with the College of Electrical and Information Engineering, Hunan University, Changsha 410082, China (e-mail: ywxhnu@gmail.com).

Yilu Liu is with the Department of Electrical Engineering and Computer Science, The University of Tennessee, Knoxville, TN 37996 USA, and also with Oak Ridge National Laboratory, Oak Ridge, TN 37831 USA (e-mail: liu@utk.edu).

Color versions of one or more figures in this article are available at <https://doi.org/10.1109/TIA.2022.3145783>.

Digital Object Identifier 10.1109/TIA.2022.3145783

0093-9994 © 2022 IEEE. Personal use is permitted, but republication/redistribution requires IEEE permission. See <https://www.ieee.org/publications/rights/index.html> for more information.

## NOMENCLATURE

ADC	Analog-to-digital converters.
AFCAs	Analog front-end circuit architectures.
AFB	Analog front-end board.
ALMA	Atacama large millimeter array.
FAST	Five-hundred-meter aperture spherical radio telescope.
FDRs	Frequency disturbance records.
FFT	Fast Fourier transform.
FPGA	Field-programmable gate array.
GBT	Green bank telescope.
GPS	Global positioning system.
PPS	Pulse per second.
PFB	Polyphase filter bank.
RF	Radio frequency.
ROACH	Reconfigurable open architecture computing hardware.
SKA	Square kilometre array.
SNAP	Smart network ADC processor.
SNR	Signal-to-noise ratio.
WAMS	Wide-area monitoring systems.

## I. INTRODUCTION

THE accuracy of synchronized timing is critical for wide-area monitoring systems (WAMSs), especially for measurement devices such as phaser measurement units (PMUs) and frequency disturbance records [1], [2]. For example, to locate power system disturbances, the calculation of electromechanical wave propagation speed distribution requires accurate synchronized sampling data in the distribution-level WAMS [3], [4]. Accurate distributed sampling can be achieved by referring to the disciplined clock reference signal, such as pulse per second (PPS) [5]. However, due to some geographical factors and the signal spoofing, near 70% PMUs faces the global positioning system (GPS) signal loss issues as reported in [6], which reduced the reliability of the WAMS.

In the past decades, numerous PMUs equipped with GPS signal receivers have been deployed on the WAMS [7]. The sampling data of PMUs are transferred based on the IEEE standard C37.118.2, where its total vector error should be lower than 1% [6]. However, the GPS signal can be maliciously defrauded and attacked and would be covered through some special equipment when the signal is weaker [8]. To solve this problem, the pulsar-based alternative timing source is proposed

for the grid measurement [9], [10]. This pulsar-based timing method claims to achieve a higher timing accuracy for the WAMS and can withstand cyberattacks. Since the pulse period of the pulsars is pretty regular and accurate, it opened a way to the timing-based studies for the relativistic two-body gravitation and timing source in grid synchronization [11]. For example, the period drift rates of the millisecond pulsars PSR B1937+214 and PSR J0437-4715 can be reached to  $6.74 \times 10^{-17} \text{ s}^{-1}$  and  $9.95 \times 10^{-18} \text{ s}^{-1}$ , respectively [12]. Therefore, the problem of sampling clock sources evolved into how to accurately extract pulse signals from the pulsars.

To achieve the extraction of pulse signals, some signal processing methods and tools are designed to efficiently process the pulsar data. In [13], two types of wavelet-based pulsar features are proposed to find the newly discovered pulsars. However, the analysis object of the wavelet method is the extracted pulses, therefore, it does not contribute to the identification of the sampling pulsar signal. To this end, some prototype tools are designed for the professional radio telescope facilities, including the Green Bank Ultimate Pulsar Processing Instrument (GUPPI) for the Green Bank Telescope (GBT) [14], PSRCRIVE for the Parkes observatory [15], and Pulsar Exploration and Search Toolkit (PRESTO) [16]. The advantages of these open-source software tools are high integration and easy to use, but the data format and embedded hardware deployment suffer from flexibility, and thus, limit their applications. To mitigate this issue, pluggable programs are needed for the real-time operation of new applications.

Based on the aforementioned considerations, some pulse extraction hardware frameworks are designed first to sample the pulsar signals. In [17], the GUPPI is developed to work with the field-programmable gate array (FPGA)-based interconnect break-out board (IBOB) and reconfigurable open architecture computing hardware (ROACH) boards, where the hardware part consists of analog-to-digital converters (ADC) and FPGA modules. As the successor to the original ROACH, the ROACH2 board is designed using the new Xilinx Virtex-6 series of FPGAs, which has a higher operating frequency and data transfer rate. One of the characters of the IBOB, ROACH, and ROACH2 is that the ADCs are all pluggable, which not only increases the flexibility but also increases the instability and complexity. In [18], the analog front-end board (AFB) is presented, which mainly includes the amplifiers, mixer, and filters. This AFB is designed for the five-hundred-meter aperture spherical radio telescope (FAST), therefore, researchers cannot verify the effectiveness of the hardware before they conduct actual tests. Moreover, the preliminary basic hardware implementation framework is built in [9], [19], and [20]. The shortcoming is that the front-end design has not been considered, which can provide direct improvement measures for system debugging and design. It is worth mentioning that there are some famous radio telescopes already established, including square kilometre array, FAST, Atacama large millimeter array, and GBT. The advantage of using radio telescopes to work with hardware frameworks is that the pulsar data are real. Nevertheless, it is not practical and convenient to use these radio telescopes for the WAMS testing during the circuit design process due to the setup cost and permission cost issues.

To this end, the analog signal generating unit scheme can be developed. For example, the dual sideband receivers with a 4-GHz analog front-end was built to test the sideband rejection of the complex astronomical signals [21]. Clear structure and reasonable parameters are selected for the designed front-end. However, it should be noted that these instruments used to generate signals that are higher than 4 GHz are expensive and rare due to their wide frequency domain. The pulsar signal belongs to the electromagnetic signal (such as X-ray), which is generated by electronic movement. A compact linear accelerator front end is designed for the free-electron lasers [22]. Fully simulating electronic motion is very expensive and complicated. Moreover, the stimulation signal based on the signal generator is usually clean and may not be able to reflect the characteristics of the real signal, including the profile and noise content. To more easily verify the usability of the pulsar-based timing source circuit, an economical but effective circuit, as well as the hardware-in-the-loop system, is required to achieve a balance between the cost of radio telescopes and the characteristics of wide-band pulsar signals. Additionally, this system is expected to produce a signal-to-noise ratio (SNR) close to the output data from the radio telescope.

To facilitate the hardware debugging process of a pulsar-based timing source, the hardware-in-the-loop simulation solution is proposed to generate simulated pulsar data and extract its pulse. This article is an extension of the IAS conference article [23]. The primary contributions of this article are as follows.

- 1) The pulse generation method is introduced to convert the real pulsar data to the analog signal. It can generate a pulse whose shape is closer to the real pulsar.
- 2) Three analog front-end circuit architectures (AFCAs) are designed to generate the analog continuous pulses for hardware debugging of the pulsar-based timing system. The advantages of the AFCAs are the simple structure, low cost, and the ability to simulate real pulsar signals.
- 3) A pulsar-based timing synchronization hardware framework is developed to provide the backup timing source for the WAMSs. The advantage is that the pulsar source can serve as the backup clock source when the GPS is not available.
- 4) Different experiments are conducted to verify the characteristics and effectiveness of these pulse generation methods and AFCAs. The results show that the period pulse is accurately extracted.

The result of this article is organized as follows: Section III introduces the steps of generating the analog pulse signal. Next, the hardware analog front-end is designed in Section IV. The timing synchronization framework is presented in Section V. After that, different experiments are presented in Section VI. Finally, Section VII concludes this article.

## II. FRAMEWORK OF ANALOG FRONT-END-BASED TIMING SYNCHRONIZATION

The proposed analog front-end-based timing synchronization is shown in Fig. 1. It can be seen that this process can be classified into the following three steps.

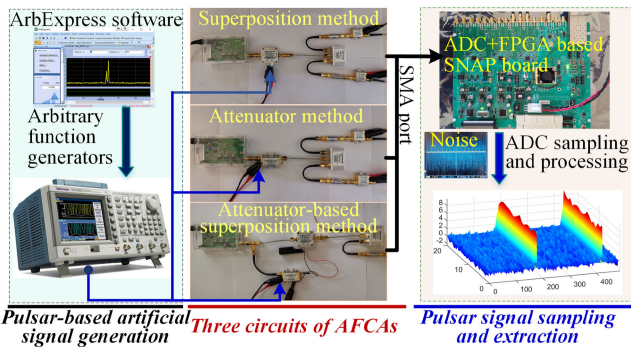


Fig. 1. Framework of the analog front-end-based timing synchronization.

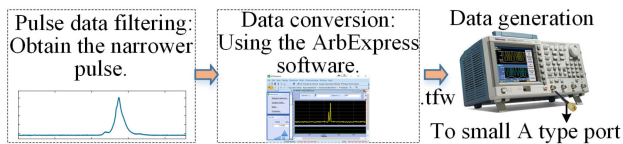


Fig. 2. Pulsar-based artificial signal generation framework.

- 1) Artificial signal generation: Utilizing the ArbExpress software and arbitrary function generators, the pulsar-based analog control signal can be generated. Then, it will be fed into the AFCA circuit as the voltage control or superimposed signal.
- 2) Circuits of AFCAs: To simulate the characteristics of real pulsar signals, three different AFCA circuits are designed to generate the analog pulse signal, including the superposition, attenuator, and attenuator-based superposition methods. The characteristics of these three circuits are explored.
- 3) Pulsar signal sampling and extraction: An FPGA-based hardware is developed to sample the analog pulsar signal. Thereafter, the pulse signal is extracted from the sampled signal using the polyphase filter bank (PFB) and data quantization.

### III. REAL PULSAR-BASED ARTIFICIAL SIGNAL GENERATION

The objective of this section is to generate pulses that are as close to the shape of the real pulse as possible. It is worth mentioning that many simulation signal sources have some built-in pulse signals. For example, the AFG3000 series arbitrary function generators can generate the rectangular pulse with a simple configuration. However, this kind of rectangular pulse does not have a pulse peak, so it is difficult to determine its period. Therefore, the real pulsar-based artificial signal generation method is introduced. The advantage of this method is that the profile, duty cycle, and period of the artificial signal is very close to the actual pulsars.

The real pulsar-based artificial signal contains three steps, including pulse data filtering, data conversion, and data generation. The pulsar-based artificial signal generation framework is shown in Fig. 2.

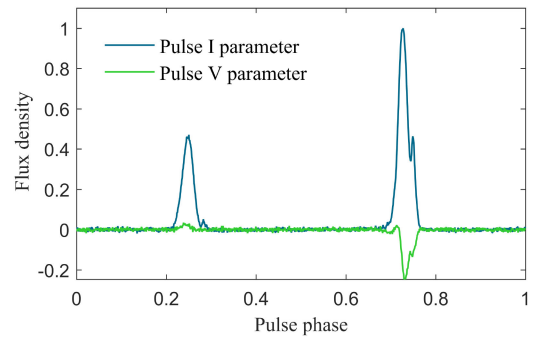


Fig. 3. Pulsar flux density of PSR B1737+21. The I and V are total intensity and circular polarization of the beam in stokes parameters.

The first step is to obtain the desired pulsar data, which is related to the radio telescope to be tested. Not all pulsars can be observed due to differences in the location and limited resolution of radio telescopes. In this section, the Skynet 20 m, an astronomical telescope with a 20-m diameter [24], is selected as an example to illustrate the detailed steps.

First, the historical observation data can be queried from the official website in [25]. Considering that the period of the millisecond pulsar (period usually less than 10 ms) is more stable [26] so that the millisecond is preferentially selected. For instance, the PSR B1737+214 can be selected as the pulsar source because the  $1 \times 10^{-17} \text{s}^{-1}$  period drift rate error can be reached [11]. The narrower pulsewidth is given priority, which is helpful for the quick debugging of the simulation because it is easier to find the peak. During the data conversion part, the pulsar profiles can be downloaded [27], as shown in Fig. 3. The difference between I and V parameters is the amplitude intensity difference. Here, the I parameter is selected because it has the largest flux density.

After obtaining the pulsar data, the ArbExpress software [28] is used to generate the specified format data for signal source, which supports *tfw*, *wfm*, and *csv* formats. Utilizing the *tfw* format pulsar data, the data generation step is implemented in the signal source by selecting the arbitrary data source. Next, the analog radio frequency (RF) signal is generated using the arbitrary data source settings of the signal source.

### IV. HARDWARE SOLUTIONS FOR ANALOG RF SIGNAL GENERATOR IN PULSAR-BASED TIMING OF THE WAMS

In this section, three types of AFCAs are designed and compared to generate the analog RF signals, including the superposition, attenuator, and attenuator-based superposition. The motivation of the RF signal generation of astronomy is to generate a pulsar signal with strong broadband noise.

#### A. RF Signal Generator Based on the Superposition Method

The sampling frequency of some ADCs is lower than 1 GHz, such as the maximum 1000 MHz is set in the SNAP board [29], so a low-bandwidth RF is designed here. The advantage of this low-bandwidth RF signal is that it does not require frequency reduction if the sampling frequency is relatively low. The first



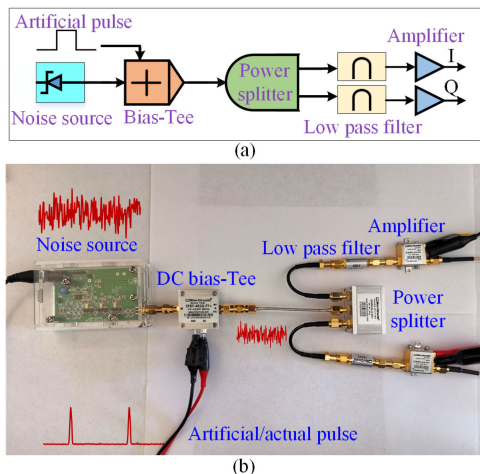


Fig. 4. RF signal generator based on the superposition method. (a) Structure of the superposition method. (b) Hardware platform of the superposition method.

designed circuit is based on the superposition method, where both the noise and pulse signals are superimposed. Therefore, it is expected to generate a noisy pulse signal, of which the designed structure is shown in Fig. 4.

As can be seen from Fig. 4(a), the noise source and the artificial signal are superimposed through the dc bias-tee. Then, a power splitter is connected after the dc bias-tee to generate two two-channel signals. There is a 90° phase difference for I and Q stokes parameters. It aims to simulate multiple channels of a radio telescope.

The hardware implementation is presented in Fig. 4(b), the BG7TBL RF noise source is used, which has 0.1 Hz to 3.5 GHz noise [30]. The artificial signal denotes the pulse signal from the real pulsar-based artificial signal generation step, with which its voltage can range from a very low value to a high value. The output of the dc bias-tee would be the sum of input voltages. This means that the pulse with noise can be generated. The low-pass filter can filter the high-frequency signal. And then, two amplifiers are used to expand the amplified voltage to fit the ADC input voltage range.

In this circuit, the pulse component belongs to the dc component. The generated pulse contains the noise and dc components. This means that the dc component may be filtered if the subsequent circuit components (amplifiers and low-pass filter) are selected inappropriately.

**B. RF Signal Generator Based on the Attenuator Method**

To address the potential problem in the first circuit scheme, an attenuator-based method is proposed. The detailed circuit and structure are shown in Fig. 5. Compared with Fig. 4, the difference is that the dc bias-tee is replaced by the attenuator. This attenuator has two inputs, one is used for noise source input, and the other is used to control the noise level. Once the pulse signal is fed into the control terminal, the voltage amplitude of noise will be retained (or slight drop) for the pulse part with a higher voltage. And the noise level will decrease sharply in the lower voltage area. Then, the pulse signal can be generated with

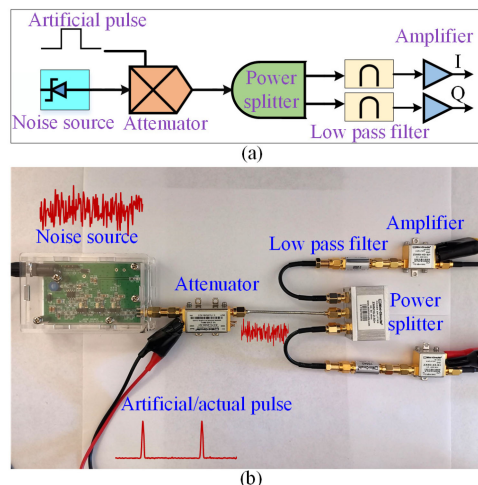


Fig. 5. RF signal generator based on the attenuator method. (a) Structure of the attenuator method. (b) Hardware platform of the attenuator method.

different voltage levels. Importantly, different noise frequency components are retained, and the analog pulse does not belong to the dc component.

In this circuit scheme, the ZX73-2500-S+ attenuator is selected [31]. The noise power of the output RF signal is controlled by the control pulse signal. A high control voltage (such as 5 V) will also result in decreased noise power based on its circuit design. This leads to the need for a strong voltage output capability of the pulse signal source, which limits the applicability.

**C. RF Signal Generator Based on the Attenuator-Based Superposition Method**

To avoid the dc component and improve the control sensitivity, the AFCA based on the attenuator-based superposition method is further proposed. This attenuator-based superposition method combines the advantages of the dc bias-tee and attenuator, whose structure is shown in Fig. 6.

It can be seen from Fig. 6(a) that the input of the dc bias-tee is based on the noise source and attenuator. Different from the circuit as Fig. 4, the dc component is replaced by the output of the attenuator. This will make the generated RF signal not contain any dc component. Compared with the scheme in Fig. 5, a dc bias-tee is used and this will make the pulse control voltage more flexible. For example, a control pulse voltage with an amplitude range of 4–5 V will output an RF signal with the desired amplitude of -4–4 V for the attenuator method. Here, the output of the noise voltage is about ±5 V. The voltage control range of the attenuator method is very narrow, causing inconvenient debugging. Instead, a control pulse voltage with an amplitude range of 0–5 V of the attenuator-based superposition method can generate the desired amplitude of -4–4 V pulse signal. It means that the control voltage is wider, so complex analog pulse signals can be generated.

Overall, considering the operating frequency range and output power level, these electronic components need to be selected appropriately to prevent signal distortion. It should be noted

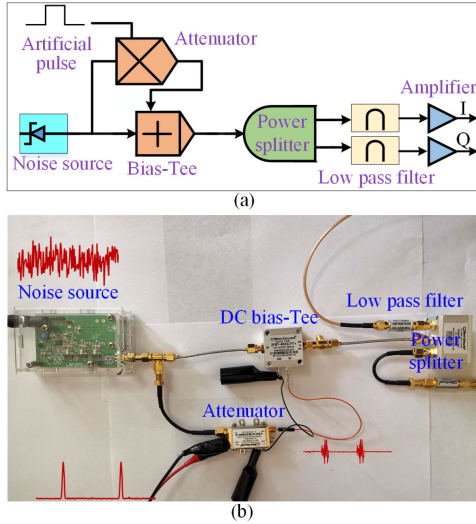


Fig. 6. RF signal generator based on the attenuator-based superposition method. (a) Structure of the attenuator-based superposition method. (b) Hardware platform of the attenuator-based superposition method.

that the simulated analog signal belongs to low frequency area, so it is recommended to select electronic components with a lower cut-off frequency. For example, the power splitter with wideband frequency from dc to 2000 MHz can be selected.

#### D. SNR Analysis

The analog circuit is expected to generate a signal similar to that of a radio telescope, such data are closer to the real pulsar signal. To evaluate the difference between the AFCA circuit and real pulsar signal, one of the critical indicators is the proportion of noise and pulse in the signal, namely the SNR.

For the AFCA circuit, the control voltage of the attenuator can be adjusted to change the SNR so that the analog signal has the same characteristics as real pulsar signals. Here, the SNR is estimated based on the generated analog pulse signals.

$$\text{SNR(dB)} = 10 \log_{10} \left( \frac{P_{\text{signal}}}{P_{\text{noise}}} \right) \quad (1)$$

where the  $P_{\text{signal}}$  and  $P_{\text{noise}}$  are the power of the analog pulse signal and noise, respectively. To estimate the SNR, the target pulse signal can be extracted by the bandpass filter, then the rest of the signal is the noise.

### V. TIMING SYNCHRONIZATION FRAMEWORK

#### A. Pulsar-Based Timing Source Hardware Framework

Based on the proposed AFCAs, the pulsar-based timing hardware framework is designed for the synchronous measurement of the WAMS, as shown in Fig. 7. In this framework, the FPGA-based SNAP is selected in which an ADC with a maximum 1000-MHz sampling frequency is embedded on the board.

As can be seen from Fig. 7, the operation can be summarized as the following three steps.

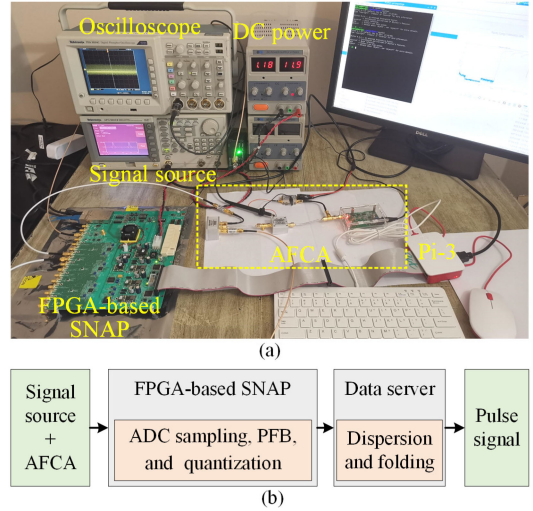


Fig. 7. Pulsar-based timing hardware framework based on the AFCA. (a) Hardware framework. (b) Pulsar signal processing method.

- 1) The artificial pulse is generated by the signal source. Combining with the noise source, these signals are then fed into the AFCA to generate two-channel analog pulse signals.
- 2) The analog pulse signal is then fed into the FPGA-based SNAP. The ADC sampling, PFB, and data quantization are executed in the SNAP board, where the PFB can be used to split the signal into multiple frequency channels [32].
- 3) Finally, the result of the PFB is sent to the data server. The dispersion and folding are implemented to extract the pulses [15]. The pulse can be used for hardware, software debugging, and precise timing for the WAMS.

#### B. Pulse Extraction Method

After sampling the data from the analog front-end, the PFB and quantization are developed to process the real-time data streaming.

The motivation of the PFB is to decompose the pulsar signal into different frequency bands. The PFB consists of a set of filterbank and the fast Fourier transform (FFT) [32]. Here, the filterbank is achieved based on the decimating polyphase filter, which means the input data are decomposed into different phases. Then, the FFT can be applied to calculate its spectrum. This process can be summarized as the following two steps:

$$y_p(n) = \sum_{m=0}^{M-1} h_p(m)x_p(n-m) \quad (2)$$

where the  $x_p$  and  $y_p$  are the input and output of the filterbank, respectively. The  $m \in M$  and  $h_p(m)$  are the number of polyphase taps and coefficients from the prototype low-pass filter, respectively.  $n$  is the sampling points. The output of the PFB can be derived as

$$Y(k, n) = \sum_{p=0}^{P-1} \sum_{m=0}^{M-1} \left[ h_p(m)e^{-2\pi i k p / P} \right] x_p(n-m) \quad (3)$$

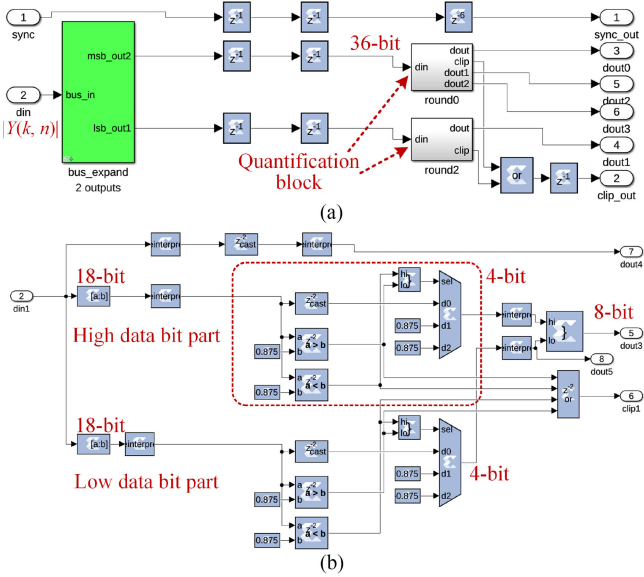


Fig. 8. Quantization module and software program. (a) Quantification for the PFB output. (b) Structure of the quantitative analysis.

where the  $P$  denotes the length of the  $y_p(n')$ . Then, the  $Y(k, n)$  can be squared to obtain its power spectrum, which can be denoted as  $|Y(k, n)|$ .

In the hardware perspective, the data bits of the  $|Y(k, n)|$  will reach 36-bit due to the multiplication and addition operations. Considering that the 10-GbE module of the SNAP can only support the 64-bit data transmission, the quantization module is necessary to increase the data efficiency because the channels of the ADC may reach 12. This means that only one channel can be exported if the data are not quantified because the number of two-channel data will exceed 64 bit. The quantization module and its corresponding software are shown in Fig. 8.

As shown in Fig. 8, the 36-bit data will first be split into two 18-bit data groups, aiming to ensure the resolution of high and low data. Then, the 18-bit data will be forcibly converted to 4-bit data with one sign bit, where the 0.875 in Fig. 8(b) is to prevent data overflow. Finally, two 4-bit data groups from the high and low data bit parts will be concatenated to form an 8-bit data group. The advantage of the quantization module is that it retains the data resolution from the high and low bit parts. Additionally, if only two ADC channels (I and V parameters) are used, the 36-bit data can be quantized to 32 bit so that 64-bit data can be formed.

Next, the quantified data will be sent to the data server, and then, the dispersion and folding will be implemented. The objective of the dispersion is to align the data of different frequency channels from the PFB results because there will be a delay for different frequency channels. The commonly used dispersion is called the incoherent dedispersion [19], its principle is to compensate for a specific time delay  $\Delta t$  for each frequency channel, which can be given by

$$\Delta t = e_{dm} (f_{cen}^{-2} - f_c^{-2}) DM \quad (4)$$

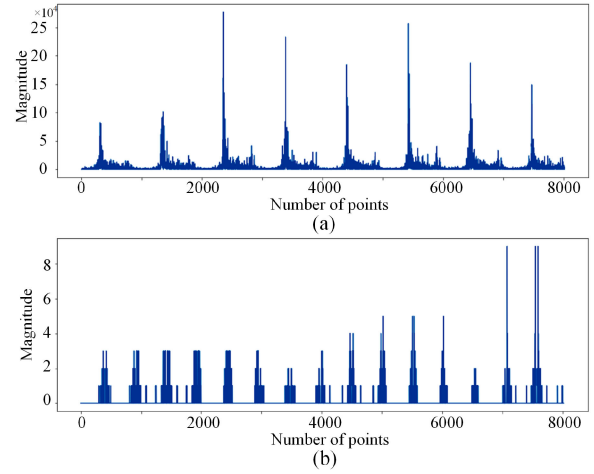


Fig. 9. Input and output of the quantitative module. (a) Input of the quantitative module. (b) Output of the quantitative module.

where the  $e_{dm}$  and  $DM$  denote the dispersion constant and dispersion measure, respectively. They can treat as the constant values for a special pulsar. The  $f_{cen}$  and the  $f_c$  are the center frequency and channel frequency in  $Y(k, n)$ , respectively. It is worth emphasizing that the dispersion is necessary for the real pulsar signal but can be ignored for the analog pulse signal generated by the AFCA since the delay cannot be simulated.

Thereafter, the folding is required after the dispersion. One of the challenges of folding is that the longer the series that folded, the more sensitive the results are to the estimation error [19]. To avoid the number of useless folding, the spectrum analysis is first conducted to estimate the period of the pulsar signal using FFT. Finally, segment folding can be achieved by adjusting the folding period.

### C. Quantitative Experimental Analysis

In this section, the quantitative experiment is conducted to verify the validity of the quantization module. The input is the output of the PFB, and the output of the quantitative module is shown in Fig. 9. It can be seen that the maximum value of Fig. 9(a) is near  $25 \times 10^4$ , which corresponds to 18 bit of data. This also means that the high 18-bit data are zero in this test. After quantification, as can be seen from Fig. 9(b), the output value is less than 10, which means that only the low 18-bit data part is quantified since the high data bit part is zero. The result manifests that the experimental results agree with the program of the quantization module.

## VI. EXPERIMENTS

To verify the validity of the proposed AFCA, different experiments are conducted using both simulated and actual data. Two types of pulsars are selected to verify the AFCAs, which consists



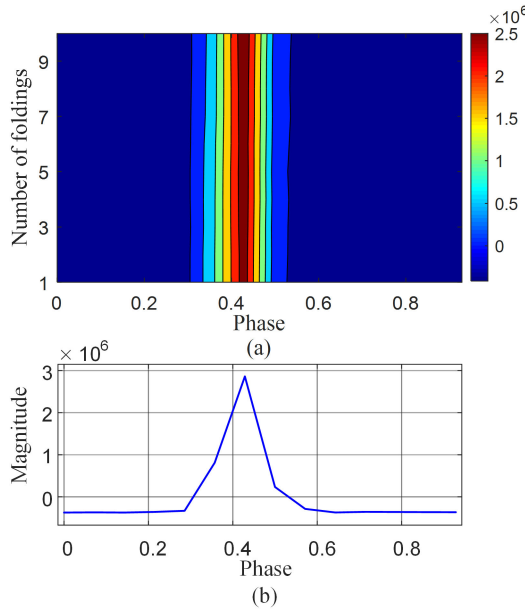


Fig. 10. Quantization module and software program.

of a binary pulsar J0055+5117<sup>1</sup> and single pulsar J1840+5640.<sup>2</sup> For a fairer comparison, the pulse signal periods are set to 5 ms, and the sampling frequency of the ADC is set to 60 MHz. An 8.29-s dataset is collected for each type of the AFCA. The taps and the order of the PFB are set to 4 and 1024, respectively. The AFG 3021B signal source is used and it has a  $\pm 1\mu\text{Hz}$  error in one year. It should be noted that the low-pass filter and the amplifier are not used since the frequency range is limited by the attenuator and its output power is sufficient.

*A. Pulse Extraction Method Verification Using Real Pulsar Data*

To verify the effectiveness of the pulse extraction method, the millisecond pulsar J1713 + 0747 is collected from the 20-m GBT located in West Virginia. A 10 min of data is collected in this test. The period of J1713 + 0747 is 4.57 ms, and the sampling time is near 3.495 ms.

Based on the proposed pulse extraction method, the extracted pulse is depicted in Fig. 10. It can be seen that the pulse is successfully extracted, as can be seen from Fig. 10(a). The maximum of the profile value of (a) is shown in Fig. 10(b). Retained by the sampling rate, the estimated period is about 0.0045699 ms with  $1.47 \times 10^{-4}\text{ms}$  error. This result can be improved by using longer time duration pulsar data. So far, the result still reveals the validity of the pulse extraction method.

*B. Pulsar-Based Artificial Signal Generation Verification*

In this experiment, the built-in simulation signal generated by a signal source and pulsar J1840+5640 signal are used to verify

<sup>1</sup>[Online]. Available: [http://www.epta.eu.org/epndb/#gl98/J0055+5117/gl98\\_1408.epn](http://www.epta.eu.org/epndb/#gl98/J0055+5117/gl98_1408.epn)

<sup>2</sup>[Online]. Available: [http://www.epta.eu.org/epndb/#gl98/J1840+5640/gl98\\_1408.epn](http://www.epta.eu.org/epndb/#gl98/J1840+5640/gl98_1408.epn)

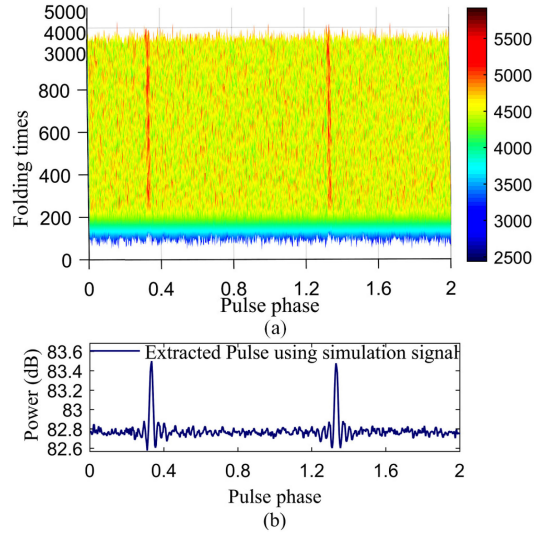


Fig. 11. Pulse extraction result using the built-in simulation pulse with attenuator method. (a) PFB result. (b) Extracted pulse after folding, it has 292 points between the pulse peaks.

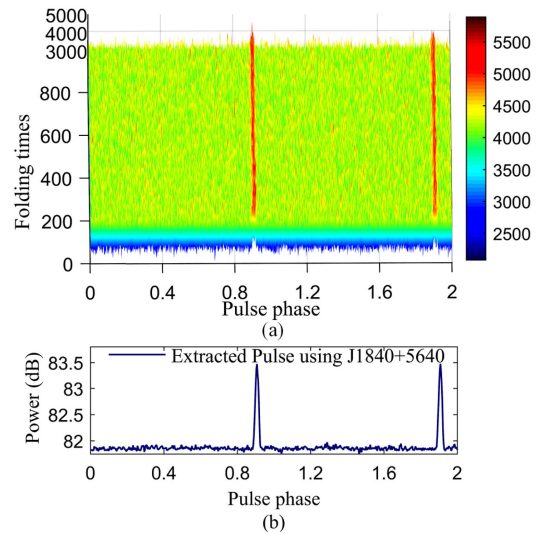


Fig. 12. Pulse extraction result using the pulsar J1840+5640 via attenuator method. (a) PFB result. (b) Extracted pulse after folding, it has 293 points between the pulse peaks.

the effectiveness of the pulsar-based artificial signal generation method. The results of the PFB and folding results are presented in Figs. 11 and 12. The  $\sin(x)/x$  model is selected for the built-in simulation scenes.

Comparing Figs. 11(a) and 12(a), it can be seen that both pulses can be extracted. However, the noise level of Fig. 11(a) is higher. And the shape of Fig. 12(b) is closer to the real pulsar scene than Fig. 11(b). Meanwhile, the expected number of points between the pulse peak should be  $60\text{MHz}/1024 \times 5\text{ms} \approx 292.97$ . Fig. 12(b) has a higher accuracy than that simulation signal because only 292 points are obtained in Fig. 11(b). The results reveal that the introduced real pulsar-based artificial signal generation can effectively generate the expected pulse.

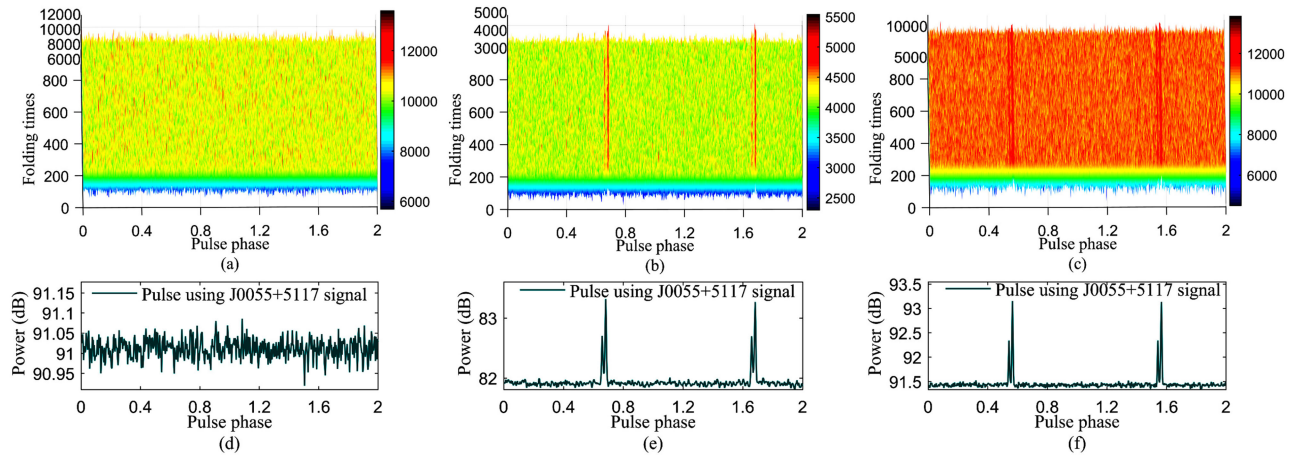


Fig. 13. Pulse extraction result using different AFCA with pulsar J0055+5117 signal. (a)–(c) PFB results of superposition, attenuator, and attenuator-based superposition methods, respectively. (d)–(f) Folding results of superposition, attenuator, and attenuator-based superposition methods, respectively. There are 293 points between the pulse peaks for (e) and (f).

### C. Performance Comparison With Different AFCAs

Based on the introduced artificial signal generation method, the AFCAs are further verified using the pulsar J0055+5117 signal, as shown in Fig. 13. It should be noted that the peak-to-peak value of the control voltage of the pulse source is set to 1 V. The control voltage of the attenuator circuit is set from 3.5 to  $-4.5$  V, and from 0 to 1 V for the attenuator-based superposition method.

Obviously, it is hard to find the pulse from the superposition circuit as shown in Fig. 13(a) and (d). The reason is that the dc component is filtered by the ADC filter circuit and the cutoff frequency of the low-pass filter. Additionally, the binary pulses are successfully extracted in Fig. 13(b) and (c). The attenuator-based superposition can extract the pulse because it does not contain the dc component compared with the superposition circuit. More importantly, the attenuator and attenuator-based superposition methods show similar shape results but with 82–83.5 dB and 91.5–93.5 dB power, respectively, as shown in Fig. 13(e) and (f). The shape and amplitude are the same compared with the real shape of J0055+5117. Since the peak-to-peak value of the control voltage is the same, the attenuator-based superposition method shows better sensitivity due to its wider power range (2 dB). However, the control voltage of the attenuator circuit should be higher than 3 V otherwise the noise level would be pretty low. This will be contrary to the characteristics of the actual pulsar signal. The control voltage of the attenuator-based superposition circuit can range from 0 to 5 V, so it has a wider adjustment range. This means that it has the potential to generate pulses with very high noise levels.

Overall, the superposition-based AFCA is suitable for occasions without filter components. The attenuator circuit is recommended to use when noise requirements are low, and it also has a low cost. The attenuator-based superposition method is recommended to use during the timing synchronization test for the WAMS, which can be a tradeoff between the cost and better pulse simulation effect.

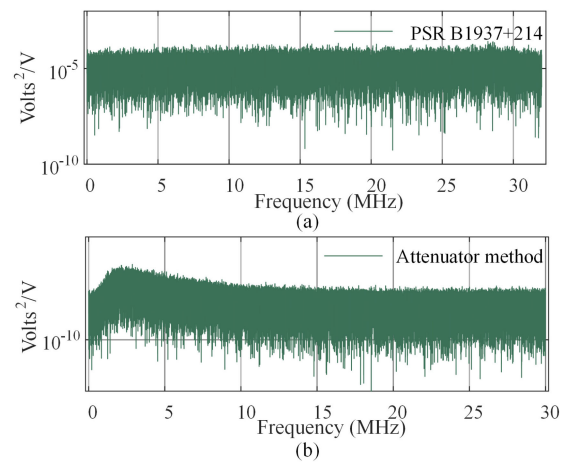


Fig. 14. Power spectral density of the collected data. (a) PSR B1937+214. (b) Attenuator method.

### D. SNR Comparison of AFCA and Real Pulsar

To compare the data difference of the AFCA and real pulsar, the SNR is calculated. Here, the attenuator method is selected and the voltage is adjusted to just extract the pulse, where the offset voltage of the control pulse signal is set to 4.6 V and the amplitude is set to 500 mV. The basis for selecting the control voltage is that the pulse can just be detected in 4.14-s data packet. The real pulsar signal comes from the PSR B1937+214, which is sampled in the Arecibo observatory in 2019. The PSR B1937+214 is one of the giant pulsars.

The power spectral density of the collected data is first analyzed, as shown in Fig. 14. It can be seen from Fig. 14(a) that the power spectral density of PSR B1937+214 is flat distribution. Compared with PSR B1937+214, the noise of the attenuator method contains more low-frequency components, which are due to the noise generator. However, the magnitude of Fig. 14(b) is lower than Fig. 14(a), this means that the attenuator method has the ability to generate weaker pulse signals even compared



TABLE I  
SNR OF ATTENUATOR METHOD AND PSR B1937+214

	Attenuator method	PSR B1937+214
SNR	-20.41 dB	-13.57 dB

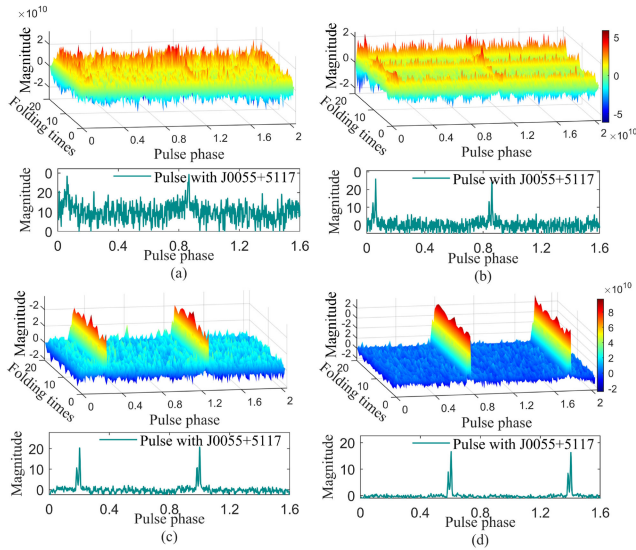


Fig. 15. PFB results and the mean pulses under different control voltage. (a) Peak-to-peak control voltage is 100 mV. (b) Peak-to-peak control voltage is 200 mV. (c) Peak-to-peak control voltage is 400 mV. (d) Peak-to-peak control voltage is 800 mV.

with the real data so that more analogy pulsar signal can be generated.

The calculated SNR results are listed in Table I. As can be seen from Table I, the result shows that the SNR value of the attenuator method is lower than the SNR of PSR B1937+214. The main reason is that the PSR B1937+214 is a giant pulsar that can emit a strong electromagnetic wave signal. This also means that the analog front-end can simulate a signal with a smaller pulse intensity.

#### E. Robustness of AFCA Against Voltage Interference

To demonstrate the robustness of the proposed AFCA circuits, experiments with different control voltages are conducted. The attenuator-based circuit is selected as an example to show the effect of voltage interference; the experiment results are presented in Fig. 15. In this test, the lowest control voltage of the pulse source is set to 3 V. The control voltage (peak voltage) of the attenuator circuit is set from 3.1 to -3.8 V. Four groups of peak-to-peak control voltages are selected including 100 mV, 200 mV, 400 mV, and 800 mV. As can be seen from Fig. 15(a), the pulse before and after folding (20th folding times) is not obvious when the peak-to-peak control voltage is 100 mV. This reason is that a lower peak-to-peak control voltage will lead to a smaller pulse amplitude difference. However, Fig. 15(c) and (d) demonstrates that when peak-to-peak control voltages are 200 and 400 mV, the profile of pulses is clear. These results indicate that the proposed AFCAs are robust when the peak-to-peak

control voltage is higher than 200 mV and may need more data to make the pulse noticeable when the voltage is lower than 100 mV.

## VII. CONCLUSION

In this article, the hardware-in-the-loop simulation solution is designed for the pulsar-based timing synchronization test of the WAMS. A pulse generation method refers to the actual pulsar signal that is introduced. The pulse extraction experiment based on the simulated and actual pulsar signal shows that the actual pulsar-based generation method is easier to determine the pulse period. Then, three AFCAs are proposed to simulate the simplified RF signal from the radio telescope. The results demonstrate that the attenuator and attenuator-based superposition AFCAs can efficiently generate accuracy analogy pulses with adjustable amplitude and wide-band noise. The result of the superposition method shows that it is not suitable for the application of the analog front-end. Meanwhile, the pulsar-based timing synchronization hardware framework is developed to provide the backup timing source when the GPS is unavailable. The quantitative analysis and real pulsar experiments show the effectiveness of the hardware framework. The SNR test results demonstrate that the proposed hardware-in-the-loop system can generate pulses with a similar SNR to that of real radio telescopes.

## REFERENCES

- [1] W. Wang *et al.*, *Information and Communication Infrastructures in Modern Wide-Area Systems*. Cham, Switzerland: Springer, 2021, pp. 71–104.
- [2] X. Deng *et al.*, “Deep learning model to detect various synchrophasor data anomalies,” *IET Gener., Transmiss. Distrib.*, vol. 14, no. 24, pp. 5739–5745, 2020.
- [3] Y. Shutang *et al.*, “Disturbance location determination based on electromechanical wave propagation in FNET/GridEye: A distribution-level wide-area measurement system,” *IET Gener., Transmiss. Distrib.*, vol. 11, no. 7, pp. 4436–4443, Dec. 2017.
- [4] K. Sun, W. Qiu, W. Yao, S. You, H. Yin, and Y. Liu, “Frequency injection based HVDC attack-defense control via squeeze-excitation double CNN,” *IEEE Trans. Power Syst.*, vol. 36, no. 6, pp. 5305–5316, Nov. 2021.
- [5] M. Q. Khan, M. M. Ahmed, A. M. A. Haidar, N. Julai, and M. K. Hasan, “Synchrophasors based wide area protection and phasor estimation: A review,” in *Proc. IEEE 7th Int. Conf. Power Energy*, 2018, pp. 215–220.
- [6] W. Yao *et al.*, “Impact of GPS signal loss and its mitigation in power system synchronized measurement devices,” *IEEE Trans. Smart Grid*, vol. 9, no. 2, pp. 1141–1149, Mar. 2018.
- [7] W. Qiu, Q. Tang, K. Zhu, W. Wang, Y. Liu, and W. Yao, “Detection of synchrophasor false data injection attack using feature interactive network,” *IEEE Trans. Smart Grid*, pp. vol. 12, no. 1, pp. 659–670, Jan. 2021.
- [8] S. Siamak, M. Dehghani, and M. Mohammadi, “Counteracting GPS spoofing attack on PMUs by dynamic state estimation,” in *Proc. Smart Grid Conf.*, 2019, pp. 1–5.
- [9] H. Yin *et al.*, “Pulsar based alternative timing source for grid synchronization and operation,” *IEEE Access*, vol. 8, pp. 147818–147826, 2020.
- [10] W. Qiu *et al.*, “Pulsar based timing for grid synchronization,” in *Proc. IEEE Ind. Appl. Soc. Annu. Meeting*, Detroit, MI, USA, 2020, pp. 1–5.
- [11] A. W. Hotan, M. Bailes, and S. M. Ord, “High-precision baseband timing of 15 millisecond pulsars,” *Monthly Notices Roy. Astronomical Soc.*, vol. 369, no. 3, pp. 1502–1520, May 2006.
- [12] J. G. Hartnett and A. N. Luiten, “Colloquium: Comparison of astrophysical and terrestrial frequency standards,” *Rev. Mod. Phys.*, vol. 83, pp. 1–9, Jan. 2011.
- [13] H. Shan *et al.*, “Wavelet based recognition for pulsar signals,” *Astron. Comput.*, vol. 11, pp. 55–63, 2015.
- [14] R. DuPlain *et al.*, “Launching GUPPI: The green bank ultimate pulsar processing instrument,” *Proc. SPIE*, vol. 7019, Aug. 2008, Art. no. 70191D.

- [15] W. van Straten, P. Demorest, and S. Osłowski, "Pulsar data analysis with PSRCHIVE," *Astronomical Res. Technol.*, vol. 9, no. 3, pp. 237–256, Jul. 2012.
- [16] S. Ransom, "PRESTO: Pulsar exploration and search Toolkit," Astrophysics Source Code Library, ascl:1107.017, Jul. 2011.
- [17] J. Ford *et al.*, "Experiences with the design and construction of wideband spectral line and pulsar instrumentation with CASPER hardware and software: The digital backend system," in *Proc. United States Nat. Committee URSI Nat. Radio Sci. Meeting*, 2014, pp. 1–1.
- [18] X.-X. Zhang, R. Duan, X.-Y. Yu, D. Li, N.-Y. Tang, and T.-C. Ching, "The design of China reconfigurable analog-digital backend for fast," *Res. Astron. Astrophys.*, vol. 20, pp. 1–10, May 2020.
- [19] X. Luo *et al.*, "Precise timing based on pulsar observation for grid synchronization," in *Proc. IEEE Power Energy Soc. Innov. Smart Grid Technol. Conf.*, 2021, pp. 1–5.
- [20] W. Qiu *et al.*, "Pulsar based timing for grid synchronization," *IEEE Trans. Ind. Appl.*, vol. 57, no. 3, pp. 2067–2076, May/June 2021.
- [21] R. Finger *et al.*, "A calibrated digital sideband separating spectrometer for radio astronomy applications," *Pub. Astronomical Soc. Pacific*, vol. 125, no. 925, pp. 263–269, Mar. 2013.
- [22] D. Angal-Kalinin *et al.*, "Design, specifications, and first beam measurements of the compact linear accelerator for research and applications front end," *Phys. Rev. Accel. Beams*, vol. 23, Apr. 2020, Art. no. 044801.
- [23] W. Qiu *et al.*, "Analog front-end: Circuit of pulsar-based timing synchronization for wams," in *Proc. IEEE Ind. Appl. Soc. Annu. Meeting*, Vancouver, BC, Canada, 2021, pp. 1–6.
- [24] G. Langston *et al.*, "UNC SKYNET adds NRAO 20 m radio telescope: Dynamic research and funding," in *Proc. Amer. Astronomical Soc. Meeting Abstr. #221*, 2013, vol. 221, Art. no. 328.07.
- [25] G. Frank *et al.*, [Online]. Available: <https://www.gb.nrao.edu/20m/>
- [26] M. T. Lam *et al.*, "The nanograv nine-year data set: Excess noise in millisecond pulsar arrival times," *Astrophysical J.*, vol. 834, no. 1, pp. 1–35, Dec. 2016.
- [27] The EPN Database of Pulsar Profiles. Univ. Manchester, Accessed: Feb. 5, 2022. [Online]. Available: <http://www.epta.eu.org/epndb/>
- [28] R. J. Cabral *et al.*, "Comparative performance of impulsive grounding systems embedded in concrete: An experiment in reduced scale," in *Proc. 33rd Int. Conf. Lightning Protection*, 2016, pp. 1–6.
- [29] G. Gancio *et al.*, "Upgraded antennas for pulsar observations in the Argentine institute of radio astronomy," *Astron. Astrophys.*, vol. 633, pp. 1–11, 2020.
- [30] L. C. Ortiz *et al.*, "Low-power dual mode MEMS resonators with PPB stability over temperature," *J. Microelectromech. Syst.*, vol. 29, no. 2, pp. 190–201, 2020.
- [31] ZX 73–2500, "Coaxial, voltage variable attenuator," Accessed: Feb. 5, 2022. [Online]. Available: <https://www.minicircuits.com/pdfs/ZX73-2500.pdf>
- [32] D. C. Price, "Spectrometers and polyphase filterbanks in radio astronomy," in *The WSPC Handbook of Astronomical Instrumentation*, Jul. 2016, Ch. 7, pp. 159–179.